Mölsä, Eemeli; Saarakkala, Seppo E.; Hinkkanen, Marko; Arkkio, Antero; Routimo, Mikko

A dynamic model for saturated induction machines with closed rotor slots and deep bars

Published in:
IEEE Transactions on Energy Conversion

DOI:
10.1109/TEC.2019.2950810

Published: 01/03/2020

Document Version
Peer-reviewed accepted author manuscript, also known as Final accepted manuscript or Post-print

Please cite the original version:
Mölsä, E., Saarakkala, S. E., Hinkkanen, M., Arkkio, A., & Routimo, M. (2020). A dynamic model for saturated induction machines with closed rotor slots and deep bars. *IEEE Transactions on Energy Conversion*, *35*(1), 157-165. Article 8889405. https://doi.org/10.1109/TEC.2019.2950810

A Dynamic Model for Saturated Induction Machines With Closed Rotor Slots and Deep Bars

Eemeli Mölsä, Seppo E. Saarakkala, Marko Hinkkanen *Senior Member, IEEE*, Antero Arkkio, and Mikko Routimo *Member, IEEE*

***Abstract*—This paper deals with a dynamic model for three-phase induction machines equipped with closed rotor slots and deep rotor bars. The thin bridges closing the rotor slots saturate highly as a function of the rotor current. The impedance of the rotor bars also varies much as a function of the rotor current frequency. An extended dynamic model, which takes into account the slot-bridge saturation and the deep-bar effect, is developed. The model extensions can be plugged into a standard machine model and parametrized easily. The proposed model can be applied to time-domain simulations, real-time control, and identification. The model is validated by means of finite-element analysis and experiments using a four-pole 5.6-kW induction machine. The results show that the accuracy of the proposed model is superior to the standard model, particularly under transient excitation typically used in standstill self-commissioning tests of induction motor drives.**

***Index Terms*—Closed rotor slots, deep-bar effect, dynamic model, induction motor, magnetic saturation, standstill identification.**

Nomenclature

Space Vectors

$\boldsymbol{u}_\mathrm{s}$	Stator voltage.
$\boldsymbol{i}_\mathrm{s}$	Stator current.
$\boldsymbol{i}_\mathrm{m}$	Magnetizing current.
$\boldsymbol{i}_\mathrm{r}$	Rotor current.
$\boldsymbol{\psi}_\mathrm{s}$	Stator flux linkage.
$\boldsymbol{\psi}_\mathrm{r}$	Rotor flux linkage.
$\boldsymbol{\psi}_{\sigma\mathrm{b}}$	Leakage flux linkage of the slot bridge.

Complex quantities are marked with boldface. Space vectors in stator coordinates are marked with the superscript s and in rotor coordinates with no superscript. Vector magnitudes are marked with non-boldface, e.g., $\psi_\mathrm{s} = |\boldsymbol{\psi}_\mathrm{s}|$.

Other Symbols

ω_m	Electrical angular speed of the rotor.
T	Electromagnetic torque.
R_s	Stator resistance.
L_s	Stator inductance.
$L_{\sigma\mathrm{b}}$	Slot-bridge leakage inductance.
$Z_\mathrm{r}(s)$	Rotor-cage impedance.
$R_{\mathrm{r}0}$	Rotor-cage resistance.
$L_{\sigma 0}$	Rotor-cage leakage inductance.
s	Differential operator $\mathrm{d}/\mathrm{d}t$.

This work was supported in part by ABB Oy Drives.

E. Mölsä, S. E. Saarakkala, M. Hinkkanen, and A. Arkkio are with the Department of Electrical Engineering and Automation, Aalto University, Espoo, Finland (e-mail: olli.molsa@aalto.fi; seppo.saarakkala@aalto.fi; marko.hinkkanen@aalto.fi; antero.arkkio@aalto.fi).

M. Routimo is with ABB Oy Drives, Helsinki, Finland (e-mail: mikko.routimo@fi.abb.com).

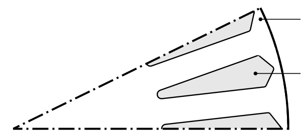

Fig. 1. Cross-section of a rotor of a 5.6-kW induction machine used as an example. The rotor slots are closed with thin bridges.

I. Introduction

THREE-PHASE induction machines are designed to operate in magnetic saturation under normal conditions. The state of saturation depends on the operating point, which may vary in a wide range in controlled drives. For the purposes of dynamic analysis and control, an induction machine is described using a space-vector model, typically expressed in the T, Π, Γ, of inverse-Γ equivalent-circuit form [1], [2]. If linear magnetics are assumed, these alternative forms are mathematically equivalent, but their nonlinear variants have fundamentally different qualities [1].

The saturation of the main flux path (the stator and rotor teeth and yokes) is comprehensively analyzed and modeled in [1], [2]. The flux densities in the stator core depend mainly on the stator flux linkage, while the flux densities in the rotor core depend on the rotor flux linkage. These saturation effects are most naturally included in the Π form [1], [2]. Since the stator core saturation dominates, the nonlinear Π model can be further reduced to the nonlinear Γ form [1]. As compared to the inverse-Γ model, advantages of the Γ model are that its saturable stator inductance can be univocally defined using a simple no-load test and that it properly takes into account the effect of the load variations on the saturation state.

A significant part of low-power three-phase induction machines are made with closed rotor slots [3], [4]. This structure has many advantages from mechanical and manufacturing point of view. Fig. 1 shows a cross-section of a typical closed-slot rotor. The thin bridges closing the rotor slots saturate highly as a function of the rotor current (i.e. electromagnetic torque), which makes these machines more complex to model as compared to the machines with open or semi-closed rotor slots. Furthermore, the eddy currents in the rotor bars make the rotor resistance and the rotor leakage inductance dependent on the frequency of the rotor current [4]–[7]. This phenomenon is called a deep-bar effect.

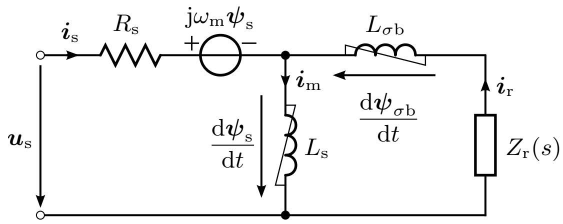

Fig. 2. Γ model including nonlinear stator inductance L_s, nonlinear slot-bridge inductance $L_{\sigma\mathrm{b}}$, and rotor-cage impedance $Z_\mathrm{r}(s)$. The model is presented in rotor coordinates.

The deep-bar effect can be included in space-vector models by means of resistor-inductor ladder circuits [7]–[11], which further can be represented in the form of a transfer function [12]. The ladder circuits in [8]–[11] are based on the multi-cage rotor structure, and they are parametrized by means of numerical optimization. The ladder circuit structure presented in [7] can be be plugged into standard space-vector models, with no need to modify the parameters of the underlying model. Furthermore, this ladder circuit can be easily parametrized by means of the standard-model parameters, if rectangular rotor bars are assumed. In [13], a ladder circuit structure similar to that in [7] has been applied to modeling the eddy-current losses of a high-frequency transformer. In order to take into account the slot-bridge saturation, the models in [8], [9], [12], [14] include a nonlinear leakage inductance. Unfortunately, these models are difficult to apply in practice due to their complexity. Furthermore, an explicit saturation model has been presented only in [14]. An experimental procedure for parametrizing the model in [12] is presented in [15]. No experimental parametrization procedures are available for the other above-mentioned models.

Including the deep-bar effect and the slot-bridge saturation in the machine model can be beneficial for self-commissioning [16], [17] and for further increasing the control performance, particularly in the field-weakening region [8]. To avoid locking the rotor, self-commissioning methods commonly apply single-phase test signals, typically either sinusoidal or stepwise, for identifying the leakage inductance and the rotor resistance [18]. Due to higher frequencies in the excitation signal, the deep-bar effect has to be taken into account. The slot-bridge saturation may also hinder these transient tests [19]. For example, if the single-phase sinusoidal voltage is fed to the stator, the bridge saturation effect distorts the rotor current waveform at low current values, which further becomes visible in the measured stator current response.

In this paper, an extended dynamic machine model is proposed, taking into account the magnetic saturation in both the stator core and the rotor slot bridges as well as the deep-bar effect. The main contributions of this paper are:

- The proposed model extensions contain only a few parameters to be selected and they are easy to plug into a standard machine model.
- A procedure for parametrization of the augmented model by means of measurements from the stator terminals is presented.
- The effect of the rotor slot-bridge saturation on the single-phase excitation is analyzed.

The model can be applied to time-domain simulations, real-time control methods, and standstill self-commissioning algorithms. The model is verified by means of experimental measurements using a 5.6-kW commercial induction machine.

II. Proposed Model

Fig. 2 shows the proposed Γ model, which includes the nonlinear stator inductance L_s, the nonlinear slot-bridge inductance $L_{\sigma\mathrm{b}}$, and the rotor-cage impedance $Z_\mathrm{r}(s)$. We have chosen the Γ model as a starting point, since it properly captures the main-flux saturation effect. Furthermore, its leakage inductance is located at the rotor side, which is a necessity for modeling the slot-bridge saturation effect. The model is presented in a coordinate system rotating at the electrical angular speed ω_m of the rotor, since the rotor-cage impedance is easiest to express in these coordinates. In the following subsections, the elements of this model are presented in detail.

A. Magnetic Saturation

We assume sinusoidally distributed windings and a uniform airgap [1], [2]. In a saturated machine, the flux densities in the stator and rotor cores are nonsinusoidally distributed in space. However, since only the fundamental space components of the flux densities link with the sinusoidally distributed windings, the space vectors can still be used to model the exact dynamics (as seen from the electrical and mechanical terminals) of the saturated machine [1].

Due to the closed rotor slots, the rotor leakage flux has an easy route via the slot bridges at low rotor currents [3]. When the rotor current (and the rotor leakage flux) increases, the thin bridges become fully saturated. Since the uniform airgap is assumed and the core losses are omitted, the saturable inductances are of the form

$$L_\mathrm{s} = L_\mathrm{s}(\psi_\mathrm{s}) \qquad L_{\sigma\mathrm{b}} = L_{\sigma\mathrm{b}}(\psi_{\sigma\mathrm{b}}) \tag{1}$$

where the saturation states depend on the flux-linkage magnitudes $\psi_\mathrm{s} = |\boldsymbol{\psi}_\mathrm{s}|$ and $\psi_{\sigma\mathrm{b}} = |\boldsymbol{\psi}_{\sigma\mathrm{b}}|$, respectively.

The saturation effects can be modeled, e.g., by defining static look-up tables for the inductances in (1). Alternatively, explicit functions can be used, which typically simplifies the implementation of the model and allows extrapolation beyond the data range used in the fitting procedure. We apply a saturation model similar to [20]–[22]

$$L_\mathrm{s}(\psi_\mathrm{s}) = \frac{L_\mathrm{su} - L_{\mathrm{s}\infty}}{1 + (\psi_\mathrm{s}/c)^r} + L_{\mathrm{s}\infty} \tag{2a}$$

$$L_{\sigma\mathrm{b}}(\psi_{\sigma\mathrm{b}}) = \frac{L_{\sigma\mathrm{bu}} - L_{\sigma\mathrm{b}\infty}}{1 + (\psi_{\sigma\mathrm{b}}/d)^s} + L_{\sigma\mathrm{b}\infty} \tag{2b}$$

where L_su and $L_{\mathrm{s}\infty}$ are the unsaturated and fully saturated values, respectively, of the stator inductance, and c and r are positive coefficients. The coefficients of the leakage inductance function in (2b) are defined similarly. Fig. 3 shows the saturation characteristics, corresponding to (2), fitted to the measured data of the 5.6-kW machine. The measurement procedure is explained in detail in Section III.

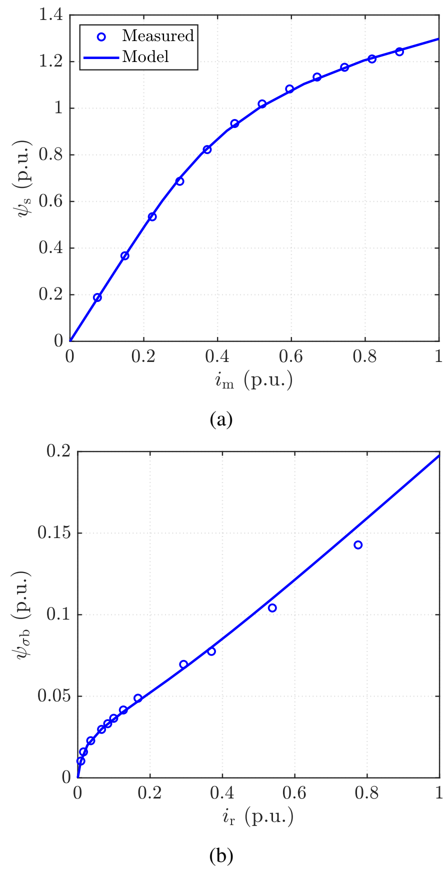

Fig. 3. Saturation characteristics for a 5.6-kW machine: (a) stator flux linkage as a function of the magnetizing current; (b) rotor leakage flux linkage as a function of the rotor current. Markers show the measured values from no-load and locked-rotor tests and the solid lines show the fitted model (2). The stator angular frequencies in the no-load test and the locked-rotor test were 0.66 p.u. and 1 p.u., respectively.

Induction machines may show some cross-saturation between the stator and leakage fluxes, especially if the rotor slots are skewed [23]. If needed, these effects could be included in the saturation model [22], at the expense of a larger number of model parameters and a more difficult identification process. The core losses are not considered in the proposed model extensions, but they are studied, e.g., in [1], [14], [24]–[26].

B. State Equations

The stator flux linkage $\boldsymbol{\psi}_{\mathrm{s}}$ and the leakage flux linkage $\boldsymbol{\psi}_{\sigma\mathrm{b}}$ are the natural choices as state variables, since the nonlinear inductances depend on these variables. Based on Fig. 2, the state equations in rotor coordinates are

$$\frac{\mathrm{d}\boldsymbol{\psi}_{\mathrm{s}}}{\mathrm{d}t} = \boldsymbol{u}_{\mathrm{s}} - R_{\mathrm{s}}\boldsymbol{i}_{\mathrm{s}} - \mathrm{j}\omega_{\mathrm{m}}\boldsymbol{\psi}_{\mathrm{s}} \tag{3a}$$

$$\frac{\mathrm{d}\boldsymbol{\psi}_{\sigma\mathrm{b}}}{\mathrm{d}t} = -\boldsymbol{u}_{\mathrm{s}} + R_{\mathrm{s}}\boldsymbol{i}_{\mathrm{s}} + \mathrm{j}\omega_{\mathrm{m}}\boldsymbol{\psi}_{\mathrm{s}} - Z_{\mathrm{r}}(s)\boldsymbol{i}_{\mathrm{r}} \tag{3b}$$

where the rotor-cage impedance is described by the transfer function $Z_{\mathrm{r}}(s)$ and $s = \mathrm{d}/\mathrm{d}t$ is the differential operator. The currents appearing in these state equations depend only on the state variables, i.e.,

$$\boldsymbol{i}_{\mathrm{r}} = \frac{\boldsymbol{\psi}_{\sigma\mathrm{b}}}{L_{\sigma\mathrm{b}}(\psi_{\sigma\mathrm{b}})} \tag{4a}$$

$$\boldsymbol{i}_{\mathrm{s}} = \frac{\boldsymbol{\psi}_{\mathrm{s}}}{L_{\mathrm{s}}(\psi_{\mathrm{s}})} - \frac{\boldsymbol{\psi}_{\sigma\mathrm{b}}}{L_{\sigma\mathrm{b}}(\psi_{\sigma\mathrm{b}})} \tag{4b}$$

The electromagnetic torque is [2]

$$T = \frac{3p}{2}\,\mathrm{Im}\left\{\boldsymbol{i}_{\mathrm{s}}\boldsymbol{\psi}_{\mathrm{s}}^{*}\right\} \tag{5}$$

where p is the number of pole pairs. Equations (2)–(5) together with the linear circuit $Z_{\mathrm{r}}(s)$ form a proper nonlinear state-space representation that can be easily implemented in simulation environments or control algorithms. The model is simplest to implement in rotor coordinates, but when needed, it can be easily transformed to any other coordinates using the standard coordinate transformations.

C. Deep-Bar Effect

Due to the eddy currents in rotor bars, the rotor resistance will increase and the rotor slot inductance will decrease as a function of the rotor current frequency. Assuming rectangular rotor bars, the rotor-cage impedance in the frequency domain is [5]–[7]

$$\boldsymbol{Z}_{\mathrm{r}}(\mathrm{j}\omega) = R_{\mathrm{r}0}\frac{\sqrt{\mathrm{j}\omega\tau}}{\tanh\sqrt{\mathrm{j}\omega\tau}} \tag{6}$$

where $\tau = 3L_{\sigma0}/R_{\mathrm{r}0}$ is the time constant, $L_{\sigma0}$ is the DC inductance, and $R_{\mathrm{r}0}$ is the DC resistance. The impedance of the end rings is omitted for simplicity.

In the time domain, the rotor-cage impedance can be modeled using various ladder circuits. The infinite-order ladder circuit shown in Fig. 4(a) corresponds to the impedance (6) if [7], [13]

$$R_{\mathrm{r}n} = (4n+1)R_{\mathrm{r}0} \tag{7a}$$

$$L_{\sigma n} = \frac{3L_{\sigma0}}{4n+3} \tag{7b}$$

where n is the number of the element. This circuit is a convenient choice for modeling the rotor-cage impedance, since it can be easily parametrized and plugged into the existing Γ model. In order to keep the transfer function $Z_{\mathrm{r}}(s)$ proper, the order of the numerator must not be higher than the order of the denominator. For this reason, the ladder circuit must be terminated with a resistor.

Fig. 4(b) compares the analytical expression (6) to the impedance of the second-order ladder circuit fitted to the measured data of the 5.6-kW machine. The measurement procedure is explained in detail in Section III. It can be seen that the second-order ladder matches very well with (6) up to the frequency of 50 Hz. If higher frequencies are of interest, the order of the ladder circuit can be easily increased using (7). For example, the fourth-order ladder yields a good accuracy up to the frequency of 400 Hz. It is to be noted that the required order depends on a particular machine via τ in (6). Furthermore, if the same ladder is applied with free parameters [without the condition (7)], the accuracy improves but also the

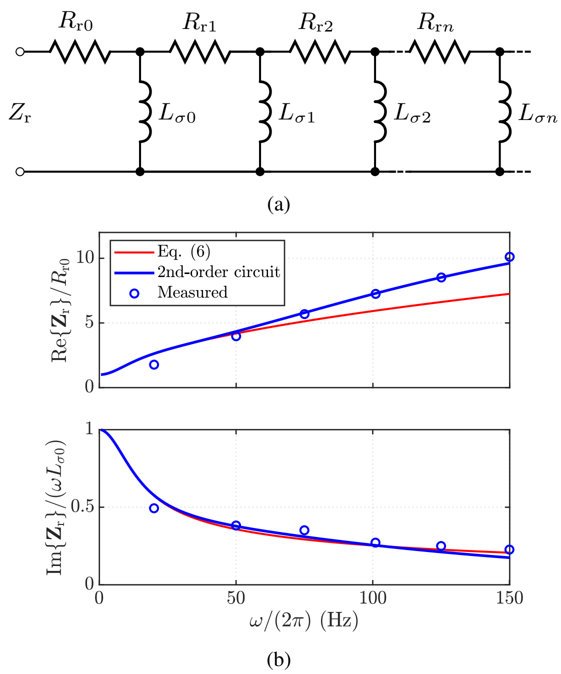

Fig. 4. Rotor-cage impedance: (a) infinite-order ladder circuit model; (b) comparison between the analytical expression (6) and its second-order ladder-circuit approximation (8). The impedances measured using the locked-rotor tests are also shown. In the measurements, the constant stator current of 0.4 p.u. was used.

amount of model parameters increases. If the model is used for predicting the losses due to pulse-width modulation or other high-frequency phenomena, the order of the ladder has to be significantly increased.

Fig. 5 shows the proposed model with the second-order ladder circuit, which is parametrized using (7). The nonlinear part $L_{\sigma b}$ of the leakage inductance takes into account the leakage flux that does not cross the rotor bars but goes through the slot bridge (or the slot opening). It is worth noticing that the effect of the stator leakage inductance, which is essentially constant, is included in $L_{\sigma b}$ and L_s. The rotor-cage impedance $Z_r(s)$ for the second-order circuit, shown in Fig. 5, is

$$Z_r(s) = \frac{15L_{\sigma 0}^2 s^2 + 140 L_{\sigma 0} R_{r0} s + 105 R_{r0}^2}{L_{\sigma 0}^2 s^2 + 35 L_{\sigma 0} R_{r0} s + 105 R_{r0}^2} R_{r0} \tag{8}$$

Assuming rectangular rotor bars, the slot leakage inductance could be estimated based on the DC rotor resistance R_{r0} and the bar height h as $L_{\sigma 0} = \sigma\mu_0 h^2 R_{r0}/3$, where σ is the conductivity of the bar and μ_0 is the permeability of the air. In this paper, the parameters R_{r0} and $L_{\sigma 0}$ are obtained by fitting the impedance $Z_r(s)$ to the measured data, i.e., no information on the machine geometry is needed for parametrizing the model.

III. Procedure for Experimental Characterization

The proposed model can be experimentally characterized from the stator terminals by means of standard three-phase tests in different steady-state operating points. In the following, the operating-point quantities corresponding to these steady-state tests are marked with the tilde. For each operating point,

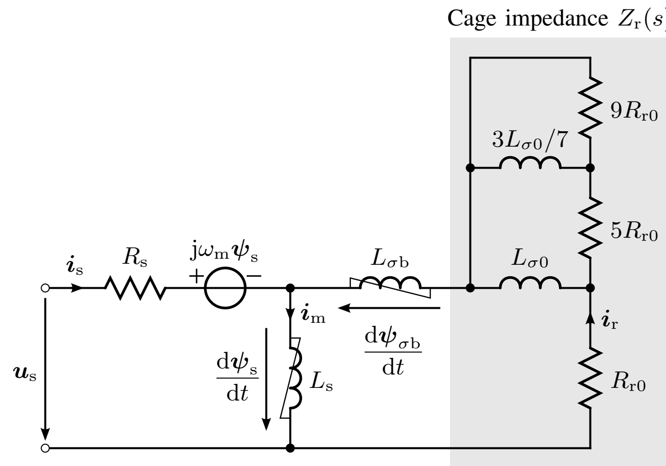

Fig. 5. Proposed Γ model including the nonlinear leakage inductance $L_{\sigma b}$ and the second-order ladder circuit for the deep-bar effect. The elements of the ladder circuit are parametrized using (7).

the fundamental voltage vector $\tilde{\boldsymbol{u}}_s$ and the fundamental current vector $\tilde{\boldsymbol{i}}_s$ are calculated from the measured time series, e.g., using the discrete Fourier transform. The stator resistance R_s can be measured simply by the DC test.

A. Stator Inductance

The main-flux saturation characteristics can be measured by completing a series of no-load tests, where the stator current magnitude is varied. For each stator current, the corresponding flux linkage is

$$\tilde{\boldsymbol{\psi}}_s = \frac{\tilde{\boldsymbol{u}}_s - R_s \tilde{\boldsymbol{i}}_s}{\mathrm{j}\omega_s} \tag{9}$$

where ω_s is the stator angular frequency. In the no-load condition, the rotor current is zero, and the stator flux linkage vector and the stator current vector are parallel. Therefore, the operating-point stator inductance can be solved from (9) as

$$\tilde{L}_s = \frac{\mathrm{Im}\left\{\tilde{\boldsymbol{u}}_s \tilde{\boldsymbol{i}}_s^*\right\}}{\omega_s \tilde{i}_s^2} \tag{10}$$

The saturation model in (2a) is fitted to the values of $\tilde{L}_s$.

B. Rotor-Cage Impedance

The rotor-side impedance can be measured by completing a series of locked-rotor tests, where the stator current magnitude is kept constant and the stator angular frequency ω_s is varied. For each angular frequency, the rotor-side impedance $\tilde{\boldsymbol{Z}}$ is defined

$$\tilde{\boldsymbol{Z}} = -\frac{\mathrm{j}\omega_s \tilde{\boldsymbol{\psi}}_s}{\tilde{\boldsymbol{i}}_r} \tag{11}$$

where the stator flux linkage is calculated using (9). The rotor current is calculated as

$$\tilde{\boldsymbol{i}}_r = \frac{\tilde{\boldsymbol{\psi}}_s}{L_s(\tilde{\psi}_s)} - \tilde{\boldsymbol{i}}_s \tag{12}$$

where $L_s = L_s(\tilde{\psi}_s)$ is already known based on the no-load tests.

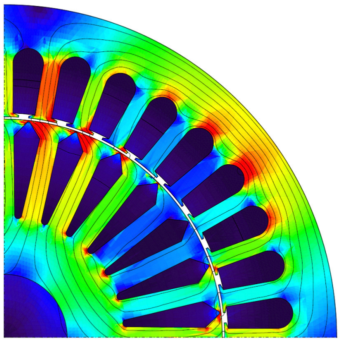

Fig. 6. Flux density distribution at nominal operating point in the cross-section of the 5.6-kW machine, computed with the finite-element method.

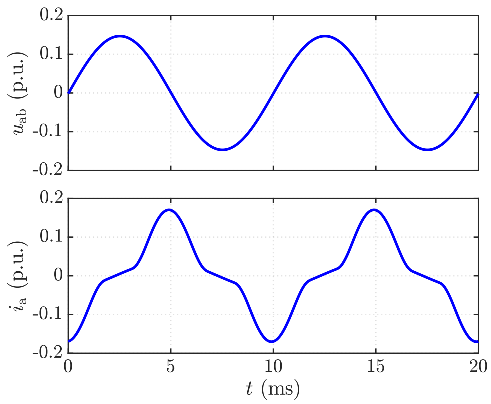

Fig. 7. Finite-element analysis result of the 100-Hz single-phase sinusoidal excitation. The test conditions correspond to Fig. 8(c).

According to the model in Fig. 5, the rotor-side impedance in the steady-state under the locked-rotor condition is

$$\boldsymbol{Z} = -\frac{\mathrm{j}\omega_{\mathrm{s}}\boldsymbol{\psi}_{\mathrm{s}}}{\boldsymbol{i}_{\mathrm{r}}} = \mathrm{j}\omega_{\mathrm{s}}L_{\sigma\mathrm{b}} + \boldsymbol{Z}_{\mathrm{r}}(\mathrm{j}\omega_{\mathrm{s}}) \tag{13}$$

where the cage impedance $\boldsymbol{Z}_{\mathrm{r}}(\mathrm{j}\omega_{\mathrm{s}})$ is given by (8). Therefore, the real part

$$\mathrm{Re}\{\boldsymbol{Z}\} = \mathrm{Re}\{\boldsymbol{Z}_{\mathrm{r}}(\mathrm{j}\omega_{\mathrm{s}})\} \tag{14}$$

depends only on $\boldsymbol{Z}_{\mathrm{r}}(\mathrm{j}\omega_{\mathrm{s}})$ but not on $L_{\sigma\mathrm{b}}$. To obtain the parameters $L_{\sigma 0}$ and $R_{\mathrm{r}0}$, the real part $\mathrm{Re}\{\boldsymbol{Z}_{\mathrm{r}}(\mathrm{j}\omega_{\mathrm{s}})\}$ of the cage impedance (8) is fitted to the measured operating-point values $\mathrm{Re}\{\tilde{\boldsymbol{Z}}\}$.

C. Slot-Bridge Inductance

Another series of the locked-rotor tests is completed. This time, the angular frequency ω_{s} is kept constant and the stator current magnitude is varied. For each current magnitude, the rotor-side impedance values are calculated using (11), as explained before. Based on (13), the operating-point slot-bridge inductance can be extracted from

$$\tilde{L}_{\sigma\mathrm{b}} = \frac{\mathrm{Im}\left\{\tilde{\boldsymbol{Z}} - \boldsymbol{Z}_{\mathrm{r}}(\mathrm{j}\omega_{\mathrm{s}})\right\}}{\omega_{\mathrm{s}}} \tag{15}$$

where the parameters of $\boldsymbol{Z}_{\mathrm{r}}(\mathrm{j}\omega_{\mathrm{s}})$ are already known based on the previous tests. The saturation model (2b) is fitted to the values of $\tilde{L}_{\sigma\mathrm{b}}$.

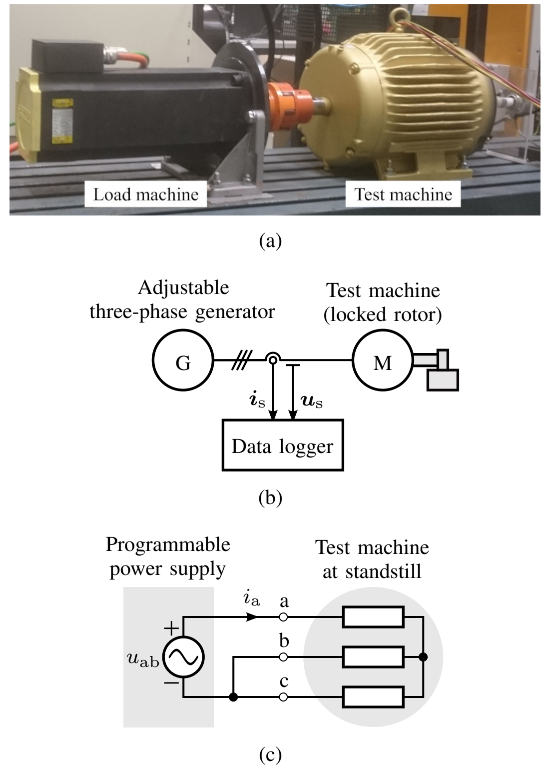

Fig. 8. Experimental setups: (a) test machine; (b) locked-rotor test; (c) single-phase excitation test at standstill. The line-to-line voltages and the phase currents are measured at the machine terminals.

TABLE I
PARAMETERS OF A 5.6-KW FOUR-POLE INDUCTION MACHINE

Stator resistance R_{s}	1.0 Ω
Stator inductance	
Unsaturated inductance L_{su}	180 mH
Fully saturated inductance $L_{\mathrm{s}\infty}$	0.03 mH
Coefficient c	1.3 $(\mathrm{Vs})^{-1}$
Coefficient r	4.7
Rotor-cage impedance	
Rotor resistance $R_{\mathrm{r}0}$	0.16 Ω
Leakage inductance $L_{\sigma 0}$	6 mH
Slot-bridge inductance	
Unsaturated inductance $L_{\sigma\mathrm{bu}}$	110 mH
Fully saturated inductance $L_{\sigma\mathrm{b}\infty}$	15 mH
Coefficient d	0.02 $(\mathrm{Vs})^{-1}$
Coefficient s	2.8

IV. FINITE-ELEMENT ANALYSIS

The slot-bridge saturation of the 5.6-kW machine is analyzed by means of finite-element simulations. Time-discretized finite-element analysis is used for solving the magnetic field of the machine [27]. Triangular, second-order isoparametric elements are used. A non-linear single-valued magnetization curve is used for the magnetization characteristics of the iron core. The field in the core region of the machine is assumed to be two-dimensional. The three-dimensional fields at the end-winding regions are taken approximately into account by adding end-winding terms in the circuit equations of the stator and rotor windings. The discretized field and circuit equations are solved together. One period of supply voltage is divided

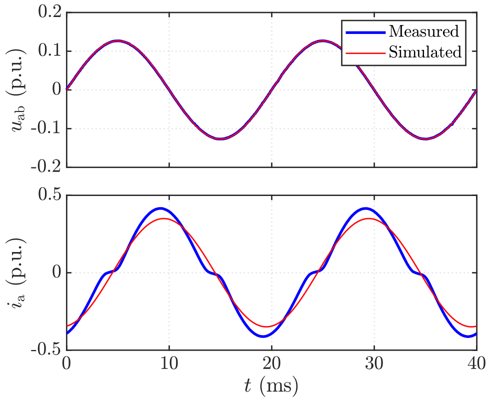

(a)

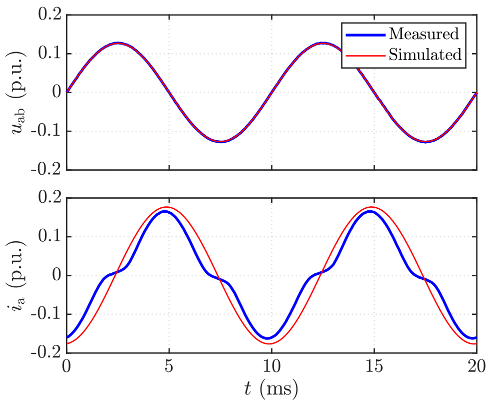

(b)

Fig. 9. Experimental results of the single-phase excitation test, together with the simulated current responses from the standard machine model. The excitation frequency is: (a) 50 Hz; (b) 100 Hz. In the model, the constant total leakage inductance is $L_{\sigma\mathrm{b}} + L_{\sigma 0} = 24$ mH, the rotor resistance is $R_{\mathrm{r0}} = 0.18\ \Omega$, and no ladder circuit is used. Other parameters are given in Table I.

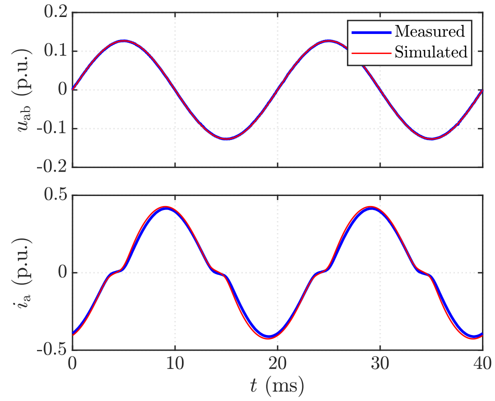

(a)

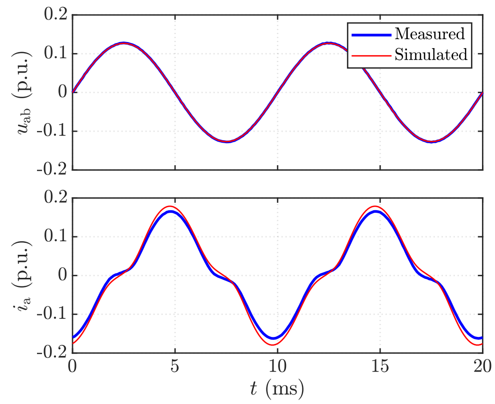

(b)

Fig. 10. Experimental results of the single-phase excitation test, together with the simulated current responses from the proposed model. The excitation frequency is: (a) 50 Hz; (b) 100 Hz. The model parameters are given in Table I.

into 300 time steps.

Fig. 6 shows the flux-density distribution in the machine cross-section at the nominal operating point. It can be seen that the slot-bridge regions saturate highly. Fig. 7 shows an example result of a single-phase excitation test at standstill, where the 100-Hz sinusoidal voltage is fed across the a and b phase terminals and the b and c terminals are short-circuited. The circuit arrangement corresponds to that in Fig. 8(c). It can be seen that the current response is highly distorted at low current values. Without the slot-bridge saturation, the current response would be sinusoidal.

V. Experimental Results

The 5.6-kW induction machine, shown in Fig. 8(a), is used in all experiments in the paper. The rated values of the machine are 60 Hz, 460 V (line-line, rms), 9.5 A (rms), and 1 770 r/min.

A. Characterization

The proposed model is characterized according to the procedure presented in Section III. In the no-load tests, a three-phase inverter, controlled by a dSPACE MicroLabBox system, supplies the induction machine. The rotor speed, stator current, and DC-link voltage are measured at the sampling frequency of 8 kHz. The stator voltage is calculated from the duty ratios and the measured DC-link voltage. A permanent-magnet load machine, mechanically coupled to the test machine as shown in Fig. 8(a), is used to regulate the shaft speed.

In the locked-rotor tests, the setup shown in Fig. 8(b) is used. The test machine is fed from an adjustable-speed synchronous generator, whose apparent power is 100 kVA. The line-to-line voltages and the phase currents are measured at the machine terminals, and the data is stored using a data logger (Dewetron DEWE-50-PCI-32) at the sampling frequency of 10 kHz.

The identified parameters of the motor model are given in Table I. Fig. 3 shows the measured operating-point flux linkages, corresponding to $\tilde{L}_{\mathrm{s}}$ and $\tilde{L}_{\sigma\mathrm{b}}$, together with the fitted saturation characteristics. Similarly, Fig. 4(b) shows the rotor-cage impedance values calculated from the measured quantities together with the fitted impedance (8).

B. Validation

1) Single-Phase Excitation Test at Standstill: In order to validate the proposed model, single-phase excitation tests at standstill, corresponding the finite-element analysis in Section IV, were measured using the experimental setup shown in Fig. 8(c). The test machine is fed by a programmable power supply (California Instruments Ametek CSW 5550). The voltage and

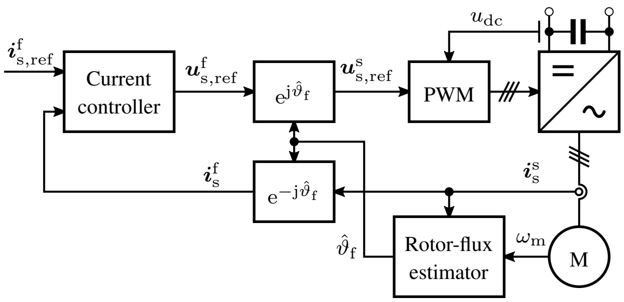

Fig. 11. Control system used in the torque-reversal test. The estimated angle of the rotor flux linkage is denoted by $\hat{\vartheta}_{\mathrm{f}}$. The DC-link voltage is denoted by u_{dc}. The vectors in estimated rotor-flux coordinates compose of d and q parts (e.g., $\boldsymbol{i}^{\mathrm{f}}_{\mathrm{s}} = i_{\mathrm{d}} + \mathrm{j}i_{\mathrm{q}}$), and are marked with the superscript f. The reference values are marked with the subscript ref.

the current are measured at the machine terminals, and the data is stored using the same data logger as in the locked-rotor tests.

Figs. 9(a) and 9(b) show the results at the excitation frequencies of 50 Hz and 100 Hz, respectively. The slot-bridge saturation effect can be clearly seen in the measured stator current waveforms. Furthermore, it can be seen that the measurement result in Fig. 9(b) matches very well with the corresponding finite-element simulation result shown in Fig. 7.

Fig. 9 also shows the corresponding simulation results, obtained with the standard Γ model, where the leakage flux saturation and the deep-bar effect are omitted (but the stator flux saturation is taken into account). The constant-valued parameters $L_{\sigma\mathrm{b}} + L_{\sigma0} = 24$ mH and $R_{\mathrm{r}0} = 0.18\ \Omega$ are the parameters at nominal operating point. The absence of the leakage flux saturation in the simulation model can be easily noticed around the zero crossings of the current. Furthermore, the simulated current amplitude decreases as a function of the frequency and differs from the measured ones, since the standard model omits the deep-bar effect.

Fig. 10 repeats the measurement results already shown in Fig. 9. The simulation results, however, are now obtained using the proposed model with the second-order ladder circuit. The parameters of the model are given in Table I. Figs. 10(a) and 10(b) show the results at the excitation frequencies of 50 Hz and 100 Hz, respectively. It can be seen that the proposed model properly captures the slot-bridge saturation effect. Furthermore, the simulated current waveform is now very close to the measured one, since the deep-bar effect is included in the model by means of the ladder circuit.

2) Torque-Reversal Test: In order to validate the proposed model with a rotating shaft, a torque-reversal test was carried out. The control system was implemented on the dSPACE system, described in Section V-A. As shown in Fig. 11, a vector controller, equipped with a current-model flux estimator, is used in the current-control mode in this test. The current controller is a proportional-integral (PI) -type controller, with the active damping and cross-coupling compensation terms [28]. The proportional and active-damping gains are 70 V/A and the integral gain is 177 500 V/As. It is important to notice that the control system is based on the standard machine model, i.e., it takes neither the bridge saturation nor the deep-bar effect into account.

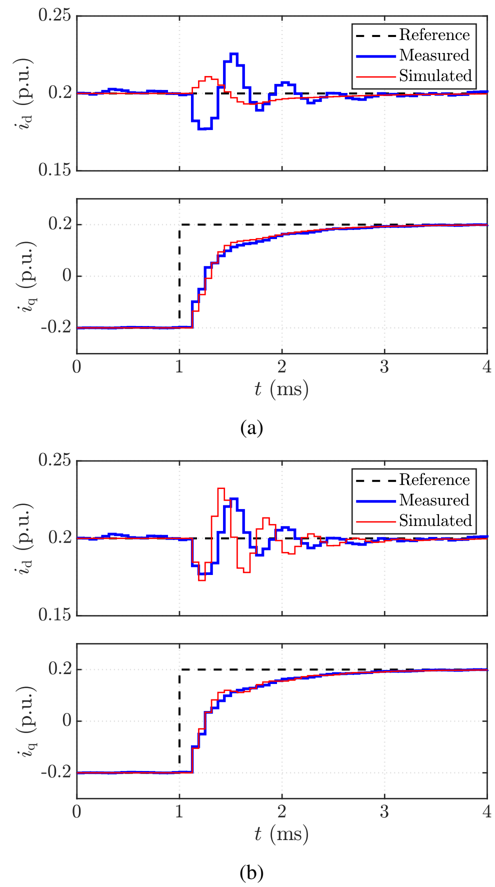

Fig. 12. Torque-reversal tests at the constant speed of 1 000 r/min: (a) standard model; (b) proposed model. The control algorithm is the same in both cases, but the plant model used in the simulations in (a) and (b) is different.

Fig. 12 shows the results of the torque-reversal test. The load machine regulates the speed at 1 000 r/min (0.66 p.u.). The flux-producing current component i_{d} and the torque-producing current component i_{q} correspond to those in the control system, i.e., they are shown in estimated rotor flux coordinates. Fig. 12(a) shows the measured and simulated waveforms, when the standard Γ model (explained in the previous subsection) is used as the plant model. The control algorithm used in the simulator equals the one used in the experiment. It can be seen that the standard model is not able to predict the cross-coupling effect in i_{d}. Fig. 12(b) repeats the same measured waveforms, but now the simulated waveforms are obtained using the proposed model as the plant model. It can be seen that the simulation result matches well with the experimental result.

VI. Conclusions

We have proposed an extended induction machine model, which takes into account the slot-bridge saturation and the deep-bar effect. The model extensions can be plugged into the standard machine model and they can be easily parametrized. The model is validated by means of finite-element analysis and experiments. The results show that the accuracy of the proposed model is superior to the standard model, particularly under single-phase excitation tests at standstill. We expect that the proposed model can be used as a basis in the development of more robust and accurate self-commissioning tests and high-performance control methods.

References

[1] G. R. Slemon, "Modelling of induction machines for electric drives," *IEEE Trans. Ind. Appl.*, vol. 25, no. 6, pp. 1126–1131, Nov./Dec. 1989.

[2] C. R. Sullivan and S. R. Sanders, "Models for induction machines with magnetic saturation of the main flux path," *IEEE Trans. Ind. Appl.*, vol. 31, no. 4, pp. 907–917, Jul./Aug. 1995.

[3] A. Boglietti, R. I. Bojoi, A. Cavagnino, P. Guglielmi, and A. Miotto, "Analysis and modeling of rotor slot enclosure effects in high-speed induction motors," *IEEE Trans. Ind. Appl.*, vol. 48, no. 4, pp. 1279–1287, Jul./Aug. 2012.

[4] S. Williamson and M. C. Begg, "Calculation of the bar resistance and leakage reactance of cage rotors with closed slots," *IEE Proc. B, Electr. Power Appl.*, vol. 132, no. 3, pp. 125–132, May 1985.

[5] J. Pyrhönen, T. Jokinen, and V. Hrabovcová, *Design of Rotating Electrical Machines*. Chippenham, UK: John Wiley & Sons, Ltd, 2008.

[6] S. Williamson and R. Schiferl, "An investigation of the influence of deep-bar effect on the resistance of cage rotor end-rings," *IEEE Trans. Ind. Appl.*, vol. IA-23, no. 4, pp. 696–704, Jul./Aug. 1987.

[7] W. Paszek, "Transientes Verhalten der Induktionsmaschine mit Hochstabläufer," *Archiv für Elektrotechnik*, vol. 63, no. 1, pp. 77–86, 1981.

[8] R. C. Healey, S. Williamson, and A. C. Smith, "Improved cage rotor models for vector controlled induction motors," *IEEE Trans. Ind. Appl.*, vol. 31, no. 4, pp. 812–822, Jul./Aug. 1995.

[9] A. C. Smith, R. C. Healey, and S. Williamson, "A transient induction motor model including saturation and deep bar effect," *IEEE Trans. Energy Convers.*, vol. 11, no. 1, pp. 8–15, Mar. 1996.

[10] J. Benzaquen, J. Rengifo, E. Albánez, and J. M. Aller, "Parameter estimation for deep-bar induction machines using instantaneous stator measurements from a direct startup," *IEEE Trans. Energy Convers.*, vol. 32, no. 2, pp. 516–524, Jun. 2017.

[11] G. Utrata, J. Rolek, and A. Kaplon, "The novel rotor flux estimation scheme based on the induction motor mathematical model including rotor deep-bar effect," *Energies*, vol. 12, no. 2676, pp. 1–21, 2019.

[12] S. D. Sudhoff, D. C. Aliprantis, B. T. Kuhn, and P. L. Chapman, "An induction machine model for predicting inverter–machine interaction," *IEEE Trans. Energy Convers.*, vol. 17, no. 2, pp. 203–210, Jun. 2002.

[13] P. G. Blanken, "A lumped winding model for use in transformer models for circuit simulation," *IEEE Trans. Power Electron.*, vol. 16, no. 3, pp. 445–460, May 2001.

[14] M. Pucci, "State-space space-vector model of the induction motor including magnetic saturation and iron losses," *IEEE Trans. Ind. Appl.*, vol. 55, no. 4, pp. 3453–3468, Jul./Aug. 2019.

[15] S. D. Sudhoff, D. C. Aliprantis, B. T. Kuhn, and P. L. Chapman, "Experimental characterization procedure for use with an advanced induction machine model," *IEEE Trans. Energy Convers.*, vol. 18, no. 1, pp. 48–56, Mar. 2003.

[16] H. A. Toliyat, E. Levi, and M. Raina, "A review of RFO induction motor parameter estimation techniques," *IEEE Trans. Energy Convers.*, vol. 18, no. 2, pp. 271–283, Jun. 2003.

[17] S. A. Odhano, P. Pescetto, H. A. A. Awan, M. Hinkkanen, G. Pellegrino, and R. Bojoi, "Parameter identification and self-commissioning in AC motor drives: A technology status review," *IEEE Trans. Power Electron.*, vol. 34, no. 4, pp. 3603–3614, Apr. 2019.

[18] R. J. Kerkman, J. D. Thunes, T. M. Rowan, and D. W. Schlegel, "A frequency-based determination of transient inductance and rotor resistance for field commissioning purposes," *IEEE Trans. Ind. Appl.*, vol. 32, no. 3, pp. 577–584, May/Jun. 1996.

[19] K. Takeuchi, M. Matsushita, Y. Tsuboi, and H. Tsutsui, "Equivalent circuit constants estimation of induction machine with a closed slot rotor by DC decay testing method," in *Proc. ICEMS*, Chiba, Japan, Nov. 2016.

[20] J. Fischer and U. Moser, "Die Nachbildung von Magnetisierungskurven durch einfache algebraische oder transzendente Funktionen," *Archiv für Electrotechnik*, vol. 42, no. 5, pp. 286–299, 1956.

[21] N. R. Klaes, "Parameter identification of an induction machine with regard to dependencies on saturation," *IEEE Trans. Ind. Appl.*, vol. 29, no. 6, pp. 1135–1140, Nov./Dec. 1993.

[22] T. Tuovinen, M. Hinkkanen, and J. Luomi, "Modeling of saturation due to main and leakage flux interaction in induction machines," *IEEE Trans. Ind. Appl.*, vol. 46, no. 3, pp. 937–945, May/Jun. 2010.

[23] C. Gerada, K. J. Bradley, M. Sumner, and P. Sewell, "Evaluation and modelling of cross saturation due to leakage flux in vector controlled induction machines," *IEEE Trans. Ind. Appl.*, vol. 43, no. 3, p. 694–702, May/Jun. 2007.

[24] S. C. Englebretson and J. L. Kirtley, "Induction motor stray losses and inter-bar currents," in *Proc. ICEM*, Vilamoura, Portugal, Sep. 2008.

[25] Z. Qu, M. Ranta, M. Hinkkanen, and J. Luomi, "Loss-minimizing flux level control of induction motor drives," *IEEE Trans. Ind. Appl.*, vol. 48, no. 3, pp. 952–961, May/Jun. 2012.

[26] D. Zhang, T. Liu, H. Zhao, and T. Wu, "An analytical iron loss calculation model of inverter-fed induction motors considering supply and slot harmonics," *IEEE Trans. Ind. Electron.*, vol. 66, no. 12, pp. 9194–9204, Dec. 2019.

[27] A. Arkkio, "Finite element analysis of cage induction motors fed by static frequency converters," *IEEE Trans. Magn.*, vol. 26, no. 2, pp. 551–554, Mar. 1990.

[28] L. Harnefors and H.-P. Nee, "Model-based current control of AC machines using the internal model control method," *IEEE Trans. Ind. Appl.*, vol. 34, no. 1, pp. 133–141, Jan./Feb. 1998.

Eemeli Mölsä received the B.Eng. degree in electrical engineering from Metropolia University of Applied Sciences, Helsinki, Finland, in 2012 and M.Sc.(Tech.) degree in electrical engineering from Aalto University, Espoo, Finland, in 2015.

He is currently working toward the D.Sc.(Tech.) degree at Aalto University. His main research interest is the control of electric drives.

Seppo E. Saarakkala received the M.Sc.(Eng.) degree in electrical engineering from the Lappeenranta University of Technology, Lappeenranta, Finland, in 2008, and the D.Sc.(Tech.) degree in electrical engineering from Aalto University, Espoo, Finland, in 2014.

He has been with the School of Electrical Engineering, Aalto University, since 2010, where he is currently a Post-Doctoral Research Scientist. His main research interests include control systems and electric drives. He was the co-recipient of the 2018 IEEE Industry Applications Society Industrial Drives Committee Best Paper Award.

Marko Hinkkanen (M'06–SM'13) received the M.Sc.(Eng.) and D.Sc.(Tech.) degrees in electrical engineering from the Helsinki University of Technology, Espoo, Finland, in 2000 and 2004, respectively.

He is currently an Associate Professor with the School of Electrical Engineering, Aalto University, Espoo, Finland. His research interests include control systems, electric drives, and power converters.

Dr. Hinkkanen was a General Co-Chair for the 2018 IEEE 9th International Symposium on Sensorless Control for Electrical Drives (SLED). He was the corecipient of the 2016 International Conference on Electrical Machines (ICEM) Brian J. Chalmers Best Paper Award and the 2016 and 2018 IEEE Industry Applications Society Industrial Drives Committee Best Paper Awards. He is an Associate Editor for the IEEE Transactions on Energy Conversions and the *IET Electric Power Applications*.

Antero Arkkio was born in Vehkalahti, Finland, in 1955. He received the M.Sc.(Tech.) and D.Sc.(Tech.) degrees from the Helsinki University of Technology, Espoo, Finland, in 1980 and 1988, respectively.

He is currently an Emeritus Professor of electrical engineering with Aalto University, Espoo. His current research interests include modeling, design, and measurement of electrical machines.

Mikko Routimo (M'18) received the M.Sc.(Eng.), Lic.Tech., and D.Sc.(Tech.) degrees in electrical engineering from the Tampere University of Technology, Tampere, Finland, in 2002, 2005, and 2009, respectively.

Since 2008, he has been with ABB Drives, Helsinki, Finland, where he is currently a Principal Engineer. Since 2017, he has also been a Professor of Practice with the School of Electrical Engineering, Aalto University, Espoo, Finland. His research interests include power electronics in power systems, control of grid-connected converters, and electric drives.